Using skew Gabor filter in source signal separation and local spectral orientation analysis

Weichuan Yu[a],*, Gerald Sommer[b], Kostas Daniilidis[c], James S. Duncan[d]

[a]*Department of Diagnostic Radiology, Yale University BML 325, P.O. Box 208042, New Haven, CT 06520-8042, USA*
[b]*Institute of Computer Science, Christian Albrechts University Preusserstrasse 1-9, D-24105 Kiel, Germany*
[c]*GRASP Lab, University of Pennsylvania 3330 Walnut Street, Levine Hall, Philadelphia, PA 19104, USA*
[d]*Department of Diagnostic Radiology and Electrical Engineering, Yale University BML 332, P.O. Box 208042, New Haven, CT 06520-8042, USA*

Abstract

Responses of Gabor wavelets in the mid-frequency space build a local spectral representation scheme with optimal properties regarding the time-frequency uncertainty principle. However, when using Gabor wavelets we observe a skewness in the mid-frequency space caused by the unsymmetrically spreading effect of Gabor wavelets. Though in most current applications the skewness does not obstruct the sampling of the spectral domain, it affects the identification and separation of source Signals from the filter response in the mid-frequency space. In this paper, we present a modification of the original Gabor filter, the skew Gabor filter, which corrects skewness so that the filter response can be described with a sum-of-Gaussians model in the mid-frequency space. The correction further enables us to use higher order moment information to analytically separate different source signal components. This provides us with an elegant framework to de-blur the filter response which is not characterized by the limited spectral resolution of other local spectral representations.
© 2004 Elsevier B.V. All rights reserved.

Keywords: Local spectral analysis; Oriented structure; Gabor wavelets; Skewness; Filter design; Source signal separation; Higher order moment information; Spectral resolution

1. Introduction

In this paper, we focus on the local spectral analysis. A filter's localization ability is measured by its support. For local signal/image analysis, a narrow filter support is desired both in the spatial domain and in the spectral domain. However, there is a limit in improving the joint localization ability according to the well-known uncertainty principle, which proves that the product of the spatial and the spectral support of an arbitrary filter has a lower bound. This lower bound can be achieved only by Gaussians and modulated Gaussians (Gabor filters) [13]. Gabor filters [13] are widely used in local image analysis [1,15,20] because of this attractive property. In addition, studies of biological vision also discovered that animal cortex can be well approximated with Gabor filters [7,19,16].

In Gabor filters, impulse responses have the same support at low and high frequencies. However, sometimes we would prefer the support to be inversely proportional to the mid-frequency, which is defined as the spectral distance between the center of the filter kernel and the spectral origin. In the time domain, for example, a low frequency signal has a relatively long duration and a high frequency signal has a relatively short duration. We wish to use a large time window to include all parts of the low frequency signal and use a small time window to better localize the high frequency signal. This inverse proportionality in the spatial domain can be ideally described as the dilation property of wavelets in the spectral domain. The coupling of the bandwidth with the mid-frequency yields Gabor wavelets, a combination of Gabor filter and wavelets [21,6], extensively used in signal analysis and image representation (e.g. [20,28]).

* Corresponding author. Tel.: +1 203 785 7294; fax: +1 203 737 4273.

E-mail addresses: weichuan.yu@yale.edu (W. Yu), gs@ks.informatik.uni-kiel.de (G. Sommer), kostas@grasp.cis.upenn.edu (K. Daniilidis), james.duncan@yale.edu (J.S. Duncan).

In the spatio-temporal orientation analysis, we also have the same motivation to keep the spectral support of the filter proportional to the mid-frequency. For example, the energy Spectrum of a constant translational motion can be characterized as an oriented plane passing through the origin in the spectral domain [1,2]. Sampling the spectrum with a set of Gabor filters at different frequencies and orientations [15] may help us to estimate the orientation of the spectral plane. Grzywacz and Yuille [14] further pointed out that the orientation uncertainty can be measured by the angle between two tangential lines, which pass through the spectral origin and embrace the spectral filter support (see Fig. 1). This angle is desired to be the same for filters centered at different frequencies in order to keep orientation estimation independent from frequency. This requires the spectral support of the filter proportional to the mid-frequency, thus justifies the applications of Gabor wavelets.

In applying Gabor wavelets, we observe a positive skewness in the mid-frequency space [14], which is caused by the unsymmetrically spreading effect of Gabor wavelets. The spreading effect and the skewness did not draw considerable attention in the computer vision community because most applications of Gabor wavelets are classification tasks. It is worth mentioning, however, that the filter response in the mid-frequency space (we call this local spectral representation the *mid-spectrum*) blurs the original local spectrum. Consequently, many frequency-based approaches suffer from the coarser resolution. For example, Gabor filters fail to recover the orientation of the well-known multiple motion planes in the spectral domain [2] in multiple motion analysis. In order to improve the resolution and even recover the original signals, deblurring techniques have been developed, which usually assume symmetric blurring of the original signals. Important applications of deblurring techniques include source signal separation
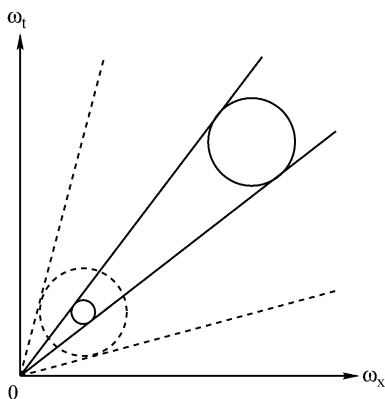

Fig. 1. The motivation for applying 2D Gabor wavelets (redrawn from [14]). We represent the spectral support of a 2D Gabor filter with a circle. The angle between two tangential lines is a measure of angular uncertainty. Applying a set of filters with constant scale may cause larger angular uncertainty at lower frequencies (as shown by the angle between two dashed lines). Thus, the spectral support of filters should be directly proportional to the mid-frequency.

and multiple spectral orientation analysis. Obviously, the skewness in applying Gabor wavelets does not fit the above symmetry assumption and makes deblurring more difficult.

This limit motivates us to correct the skewness in the mid-spectrum. The correction facilitates the deblurring of filter responses so that we no more suffer from the limited resolution of frequency-based approaches. The rest of the paper is organized as follows: Section 2 studies the skewness in detail and proposes a new filter to correct the skewness in the mid-spectrum. In Section 3, we further describe the corrected mid-spectrum with a sum-of-Gaussians model and use higher order moment information to identify and separate different 1D source signals. The deblurring of the mid-spectrum is also demonstrated. In Section 4, we extend the analysis to 2D spectral orientation analysis. Section 5 presents some experiments to evaluate the comparison between the new filter and Gabor wavelets. This paper is concluded in Section 6.

2. Skew Gabor filter

2.1. The skewness of gabor wavelets

We first analyze the positive skewness in applying Gabor wavelets. For simplicity we begin with a 1D Gabor filter whose impulse response reads

$$g_1(x; \omega_0, \sigma_x) = \frac{1}{\sqrt{2\pi}\sigma_x} e^{-(x^2/2\sigma_x^2)} e^{j\omega_0 x}. \tag{1}$$

Here ω_0 denotes the mid-frequency and σ_x is the scale parameter. The spectrum of $g_1(x; \omega_0, \sigma_x)$ is a Gaussian centered at ω_0

$$G_1(\omega; \omega_0, \sigma_x) = e^{(-\sigma_x^2(\omega-\omega_0)^2/2)} \tag{2}$$

with bandwidth inversely proportional to σ_x. In local signal analysis, we usually calculate the spatial convolution between $g_1(x; \omega_0, \sigma_x)$ and the signal $i(x)$ (here * denotes convolution)

$$h_1(x; \omega_0, \sigma_x) = i(x) * g_1(x) = \int_{\xi=-\infty}^{\infty} i(\xi) g_1(x - \xi) d\xi, \tag{3}$$

where the Gaussian envelope of $g_1(x)$ defines the local neighborhood, although we still let $d\xi$ go from $-\infty$ to ∞ for simplicity. At a fixed position x_0, the filter response is simplified as an inner product

$$h_1(x_0; \omega_0, \sigma_x) = \int_{\xi=-\infty}^{\infty} i(\xi) g_1(x_0 - \xi) d\xi. \tag{4}$$

Using the facts that $g_1(x_0 - x) = g_1^*(x - x_0)$ and $G_1^*(\omega) = G_1(\omega)$ (here * denotes conjugation) and the Parseval theorem ([4], pp. 113–115), the above inner product can

also be represented in the spectral domain as follows

$$h_1(x_0; \omega_0, \sigma_x) = \int_{\xi=-\infty}^{\infty} I(\omega)G_1(\omega)e^{j\omega x_0} d\omega. \tag{5}$$

Here $I(\omega)$ is the spectrum of $i(x)$. Thus, at $x=x_0$ (for simplicity we may set $x_0=0$) we obtain a local spectral representation of the original signal, which is a function of the mid-frequency ω_0 and the scale σ_x. We call this local spectral representation the mid-spectrum.

The mid-spectrum $h_1(\omega_0, \sigma_x)$ spreads every spectral Dirac component of the source signal into a function of ω_0 and therefore blurs the spectrum of the original signal. Assume that the spectrum of the source signal is a Dirac function $I(\omega)=\delta(\omega-\omega_i)$ originating from a complex harmonic. Its mid-spectrum turns out to be

$$h_1(\omega_0, \sigma_x) = G_1(\omega_i; \omega_0, \sigma_x) = e^{(-\sigma_x^2(\omega_0-\omega_i)^2/2)}. \tag{6}$$

If the parameter σ_x is a constant, then $h_1(\omega_0, \sigma_x)$ is a Gaussian spreading of $\delta(\omega-\omega_i)$ and there is no skewness. However, if the wavelet property is preferred, i.e. σ_x is inversely proportional to ω_0

$$\sigma_x = \frac{C}{\omega_0} \tag{7}$$

with C as a constant. Then, we obtain the positive skewness of ω_0 [14] (see also Fig. 2)

$$h_1(\omega_0, C) = e^{(-C^2(\omega_0-\omega_i)^2/2\omega_0^2)}. \tag{8}$$

We may straightforwardly extend the above analysis to n-dimensional Gabor wavelets with isotropic envelope. For 2D Gabor wavelets in the spatio-temporal domain we have the following relation

$$\sigma_x = \sigma_t = \frac{C}{\sqrt{\omega_{x0}^2 + \omega_{t0}^2}}. \tag{9}$$

The mid-spectrum of a 2D impulse $\delta(\omega_{x0}-\omega_{xi}, \omega_{t0}-\omega_{ti})$ then reads

$$h_2(\omega_{x0}, \omega_{t0}, C)$$
$$= \exp\left\{-\frac{C^2[(\omega_{x0}-\omega_{xi})^2 + (\omega_{t0}-\omega_{ti})^2]}{2(\omega_{x0}^2 + \omega_{t0}^2)}\right\}. \tag{10}$$

Fig. 2 displays two skewness examples of 1D- and 2D-Gabor wavelets.

In many Gabor wavelets approaches, this skewness is harmless because it does not obstruct the descriptions of different signals with a set of samples [18,22]. Thus, the main attention was attracted to the efficient covering/sampling of the spectrum as well as the coefficient estimation of the Gabor basis [3,20,28]. But we should keep in mind that the Gabor wavelets filtering (see Eq. (8) and Fig. 2) really blurs the input signal in the mid-frequency space. As a result, the spectral resolution in the mid-spectrum is much worse than that in the original signal. More importantly, the non-symmetric blurring in the Gabor wavelets further hampers the possible application of deblurring techniques, which work well only under the assumption of symmetric blurring. In order to apply deblurring techniques in the mid-spectrum and eventually use the mid-spectrum in source signal separation and multiple-orientation analysis, we need to correct the skewness in Gabor wavelets.

2.2. Correcting the skewness with skew Gabor filter

The positive skewness in Eq (8) is caused by the term ω_0^2 in the denominator of the exponential function. In order to remove ω_0^2 from the denominator, we design a new *skew Gabor filter* whose spectral definition reads

$$SG_1(\omega; \omega_0, C) = \exp\left\{-\left(\frac{C^2}{2}\right)\left(\frac{\omega-\omega_0}{\omega}\right)^2\right\}. \tag{11}$$
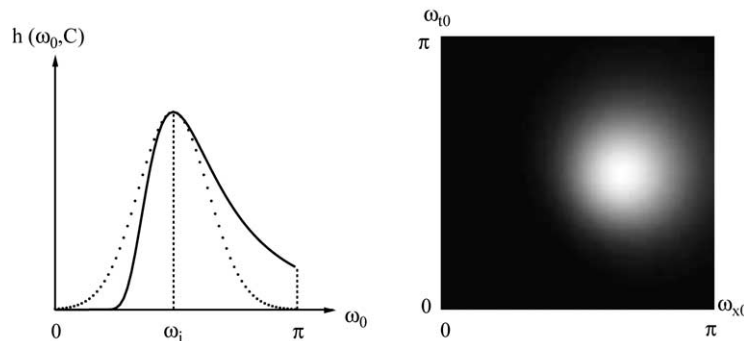

Fig. 2. The skewness of Gabor wavelets. Left: The solid curve is $h_1(\omega_0, C)$ in Eq. (6) and the dotted curve is a Gaussian function centered at ω_i with the scale parameter ω_i/C. $C=3.5$, $\omega_i=\pi/2$. Right: 2D skewness $h_2(\omega_{x0}, \omega_{t0}, C)$ in Eq. (10). $C=3.5$, $\omega_{xi}=2\pi/3$, $\omega_{ti}=\pi/2$. In both cases, Gabor wavelets blur the input Dirac function into a widely-spreading function.
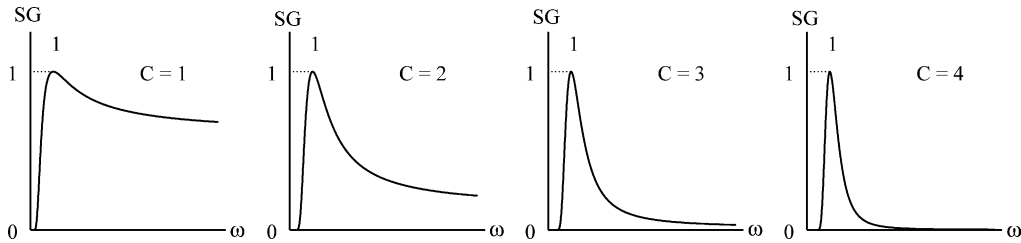
Fig. 3. Spectra of skew Gabor filters with different C value. With $C \geq 3$, $\lim_{\omega \to \infty} SG_1(\omega; \omega_0, C)$ is close to zero. $\omega_0 = \pi/2$.

Replacing the function $G_1(\omega; \omega_0, \sigma_x)$ in Eq. (5) with $SG_1(\omega; \omega_0, \sigma_x)$ yields

$$sh_1(\omega_0, C) = \exp\left\{ -\frac{C^2(\omega_0 - \omega_i)^2}{2\omega_i^2} \right\}. \tag{12}$$

The new mid-spectrum is then an ideal Gaussian with its scale parameter proportional to the mean value ω_i. The symmetry in the mid-spectrum is therefore achieved using the new filter. The spectral shape of the skew Gabor filter, especially the tail of the filter depends very much on the value of C since

$$\lim_{\omega \to \infty} SG_1(\omega; \omega_0, C) = e^{(-C^2/2)}. \tag{13}$$

From Fig. 3 it is clear to see that larger C values make the tail of the filter closer to zero, which means that the filter is more likely to have finite energy in the spectral domain. Thus, a large C value is preferred in order to simplify the application of the Fourier theory. On the other hand, however, a large C value also needs large filter kernel in the spatial domain. Obviously,

the filter kernel could not be arbitrarily large in many local image analysis applications. To make a compromise, we must choose a reasonable C value. It is easy to find out that when $C = 3.5$, the amplitude of $e^{(-C^2/2)}$ is about 0.22% of the maximal spectral amplitude of the filter at ω_0 and can be considered as approximately negligible. Thus, we choose $C = 3.5$ in this paper.

The spatial definition of the skew Gabor filter $sg_1(x)$ has no analytical expression because there is no closed-form representation of the inverse Fourier transform of $SG_1(\omega)$. We may obtain an FIR version of both the real and the imaginary part of the skew Gabor filter $sg_1(x)$ using an FIR window in the Fourier domain and discrete Fourier transform (DFT). In Fig. 4 we display one example of the skew Gabor filter. Although the skew Gabor filter decays more slowly in the spatial domain than the Gabor filter, the energy primarily lies inside the central part of the Gaussian envelope (i.e. between -12 and 12 on the left side in Fig. 4). If we extract the central part of the plot as an FIR filter, the energy loss is negligible.
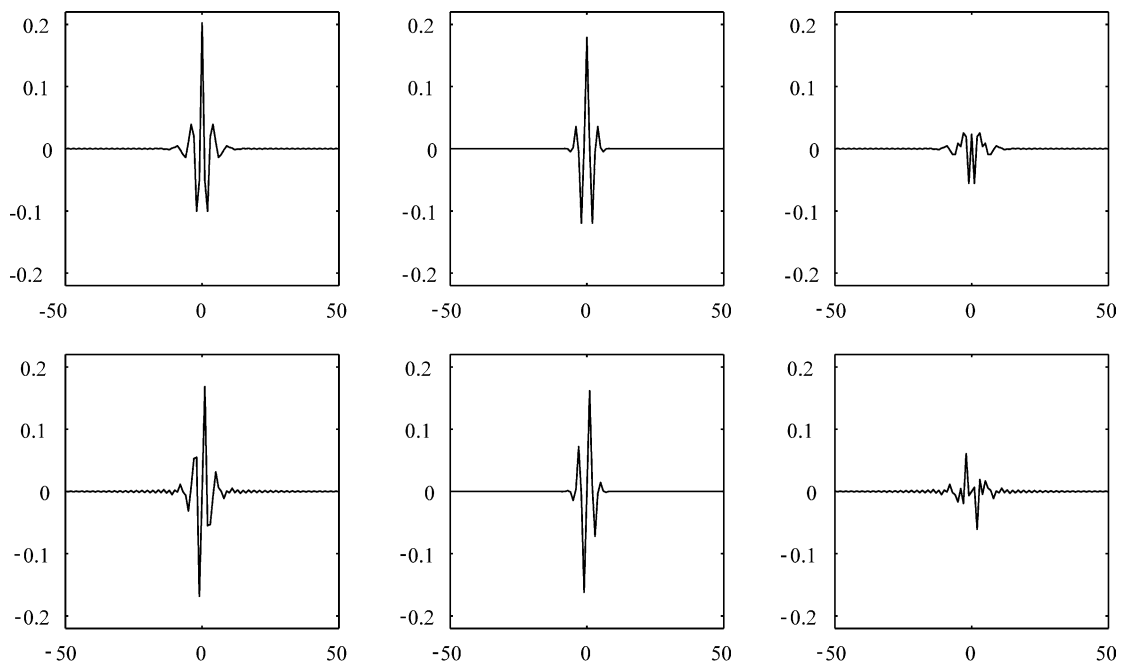

Fig. 4. Top: The real parts of a 1D skew Gabor filter (left) and a Gabor filter (middle) as well as their even-symmetric difference (right). Bottom, The imaginary parts of both filters (left, skew Gabor; middle: Gabor) and their odd-symmetric difference (right). The parameters are $C = 3.5$ and $\omega_0 = \pi/2$.
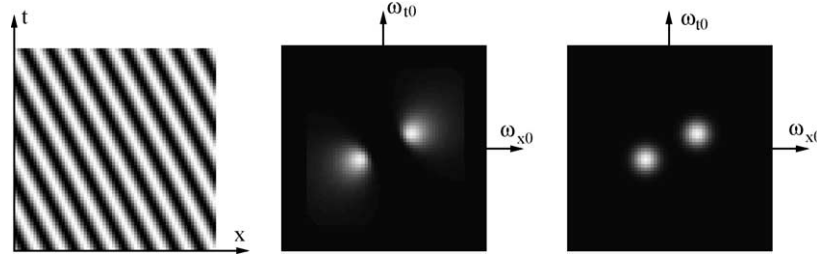
Fig. 5. Left, 1D cosine sequence $f(x,t) = 5\cos(\pi/4(x+0.5t))$. Middle: Mid-spectrum using Gabor wavelets with $C = 3.5$. Right, Mid-spectrum using 2D skew Gabor filters with the same C. The skewness in the middle image is corrected.

Similarly, we may correct the skewness of 2D Gabor wavelets by using a 2D skew Gabor filter

$$SG_2(\omega_x, \omega_t; \omega_{x0}, \omega_{t0}, C)$$

$$= \exp\left\{ -\left(\frac{C^2}{2}\right)\left[\frac{(\omega_x - \omega_{x0})^2 + (\omega_t - \omega_{t0})^2}{\omega_x^2 + \omega_t^2}\right]\right\}. \quad (14)$$

The mid-spectrum corresponding to $\delta(\omega_{x0} - \omega_{xi}, \omega_{t0} - \omega_{ti})$ is then a 2D Gaussian centered at $(\omega_{xi}, \omega_{ti})$

$$sh_2(\omega_{x0}, \omega_{t0}, C)$$

$$= \exp\left\{ -\left(\frac{C^2}{2}\right)\left[\frac{(\omega_{x0} - \omega_{xi})^2 + (\omega_{t0} - \omega_{ti})^2}{\omega_{xi}^2 + \omega_{ti}^2}\right]\right\}. \quad (15)$$

Fig. 5 shows an example of a 1D cosine sequence. We apply both Gabor wavelets and skew Gabor filters to obtain local spectral representation. Clearly, the positive skewness in the mid-spectrum using Gabor wavelets is corrected by using the skew Gabor filters. Here we use only one constant C to keep the Gaussian envelope isotropic. We may also apply two different constants (i.e. $C_x \neq C_t$) to form a mid-spectrum with an elongated Gaussian shape. But this is beyond the scope of this paper.

3. 1D source signal separation

In this section, we demonstrate the merit of correcting the positive skewness in 1D source signal separation. Assume

we have a source signal $s(x)$ in the spatial domain whose local spectrum $S(\omega)$ consists of two Dirac components

$$S(\omega) = a_1\delta(\omega - \mu_1) + a_2\delta(\omega - \mu_2), \quad (16)$$

where a_1 and a_2 denote their amplitudes and μ_1 and μ_2 denote their offsets. Our goal is to estimate these amplitudes and offsets from the local mid-spectrum so that the source components can be identified and separated. Here we provide such a simple example with known parameters to simplify the comparison between Gabor wavelets and skew Gabor filters. Our focus is the comparison between two different local spectral analysis methods. Certainly the traditional Fourier analysis can easily deal with such a simple spectrum. But the traditional Fourier transform also has to face the poor localization ability in the spatial domain, aliasing problem in the sampling, and block effect in extracting a Fourier window. Actually, it was these problems that make the local spectral analysis methods attractive since they provide solutions to these problems.

If we apply plain Gabor wavelets for filtering, the mid-spectrum is an overlap of two skewness curves (cf. Fig. 6)

$$h_0(\omega_0) = a_1 e^{(-C^2(\omega_0 - \mu_1)^2/2\omega_0^2)} + a_2 e^{(-C^2(\omega_0 - \mu_2)^2/2\omega_0^2)}. \quad (17)$$

No analytic approach is available to extract those four parameters from the skewness curve. Though iterative algorithms (e.g. [8,24]) or learning methods (e.g. [9]) may be used to extract the desired parameters, these non-analytic approaches are computationally inefficient and are sensitive to initial values and parameter setting in the cost function.
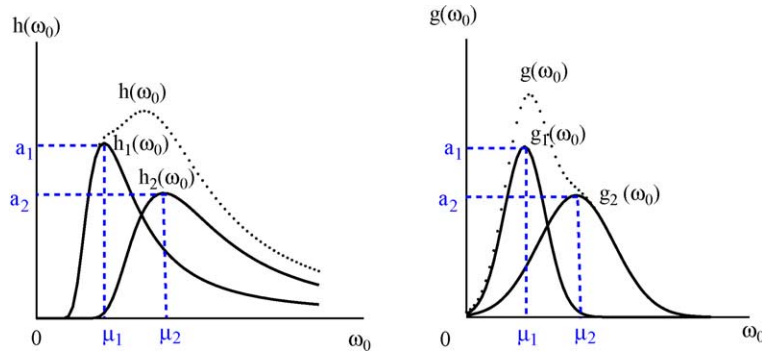

Fig. 6. Left: The mid-spectrum after Gabor wavelets filtering is an overlap of two skewness curves. Right, The superposition of two Gaussians after 1D skew Gabor filtering. We have totally four unknowns: the amplitudes a_1 and a_2, and the mean values μ_1 and μ_2. The scale parameters of these two Gaussians are determined by μ_1/C and μ_2/C, respectively.

Further, they are susceptible to local minima in the regression procedure. Thus, we prefer to have an analytic framework for parameter regression.

The correction of skewness makes this idea possible. Under the same assumption as that in Eq. (16), the mid-spectrum after skew Gabor filtering is then a sum of two differently weighted and shifted Gaussian functions (for simplicity we omit the coefficient term $(1/\sqrt{2\pi}\sigma)$ of the Gaussian)

$$g(\omega_0) = g_1(\omega_0) + g_2(\omega_0) \tag{18}$$

with

$$\begin{cases} g_1(\omega_0) = a_1 e^{-(\omega_0 - \mu_1)^2/2(\mu_1/C)^2} \\ g_2(\omega_0) = a_2 e^{-(\omega_0 - \mu_2)^2/2(\mu_2/C)^2} \end{cases} \tag{19}$$

In above Gaussians the scale parameters are proportional to the mean values. In Fig. 6 we demonstrate the mid-spectrum of skew Gabor filtering, which is an overlap of two Gaussian curves.

The sum-of-Gaussians model is well studied from the statistical aspect and is widely-used in neural network approaches (e.g. [9,24]). One benefit of this model is that we are able to use higher order moment information to extract parameters. According to Appendix A, we obtain the following system of equations in a_1, a_2, μ_1, and μ_2

$$\begin{cases} a_1\mu_1 + a_2\mu_2 = m_0 \dfrac{C}{\sqrt{2\pi}} = b_1 \\ a_1\mu_1^2 + a_2\mu_2^2 = m_1 b_1 = b_2 \\ a_1\mu_1^3 + a_2\mu_2^3 = \dfrac{1}{\frac{1}{C^2} + 1} m_2 b_1 = b_3 \\ a_1\mu_1^4 + a_2\mu_2^4 = \dfrac{1}{\frac{3}{C^2} + 1} m_3 b_1 = b_4 \end{cases} \tag{20}$$

Here m_0 denotes the integration of $g(\omega_0)$ and m_1, m_2, and m_3 denote the first three order moments of $g(\omega_0)/m_0$. Solving these equations (Appendix B) yields

$$\begin{cases} a_1 = \dfrac{a(2ab_2 + bb_1 + b_1\sqrt{b^2 - 4ac})}{b^2 - 4ac - b\sqrt{b^2 - 4ac}} \\ a_2 = \dfrac{a(2ab_2 + bb_1 - b_1\sqrt{b^2 - 4ac})}{b^2 - 4ac + b\sqrt{b^2 - 4ac}} \\ \mu_1 = \dfrac{-b + \sqrt{b^2 - 4ac}}{2a} \\ \mu_2 = \dfrac{-b - \sqrt{b^2 - 4ac}}{2a} \end{cases} \tag{21}$$

where b_1, b_2, b_3, and b_4 are defined in (20) and the variables a, b, and c are defined as

$$\begin{cases} a = b_2^2 - b_1 b_3 \\ b = b_1 b_4 - b_2 b_3 . \\ c = b_3^2 - b_2 b_4 \end{cases} \tag{22}$$

The term $b^2 - 4ac$ is guaranteed to be no less than zero (see Appendix B). If $b^2 - 4ac = 0$, there is only one single Gaussian (i.e. $\mu_1 = \mu_2$) and we can estimate its mean value and amplitude by using Eqs. (A1) and (A2).

In Fig. 7, we display a concrete example of source signal separation. The source signal is composed of two cosine functions

$$s(x) = 2\cos\left(\frac{\pi}{4}x\right) + \cos\left(\frac{3\pi}{8}x\right) \tag{23}$$

with the spectrum

$$S(\omega) = \delta\left(\omega \pm \frac{\pi}{4}\right) + \frac{1}{2}\delta\left(\omega \pm \frac{3\pi}{8}\right),$$
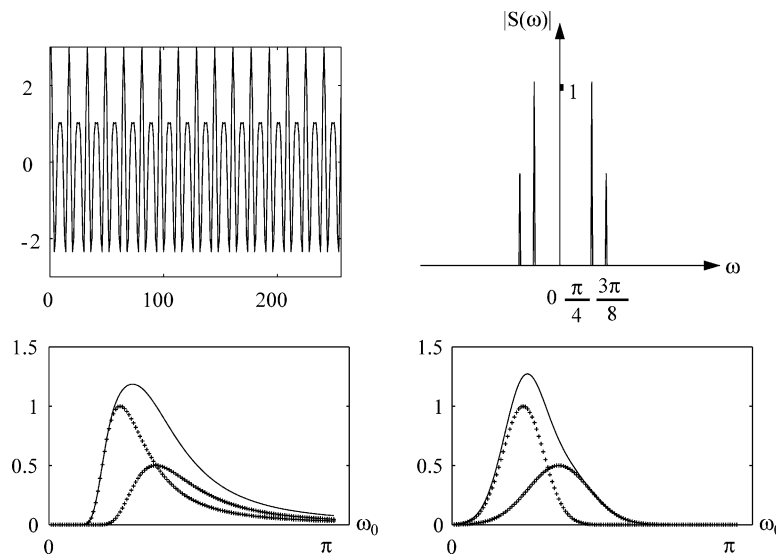

Fig. 7. Top: The source signal and its energy spectrum. Bottom: The positive mid-spectra (solid lines) using Gabor wavelets (left) and using skew Gabor filters (right). These curves are actually overlapping of the spreading responses of two Dirac functions (shown as crosses). $C=3.5$.

Table 1
Estimation results on Mid-Spectra using Gabor wavelets and skew Gabor filters

Parameter	True value	Gabor wavelets	Skew gabor filter
a_1	1	1.1451	0.9976
a_2	0.5	0.2870	0.4825
μ_1	$\pi/4 = 0.7854$	1.0814	0.8130
μ_2	$3\pi/8 = 1.1781$	1.7965	1.2079

For comparison we apply the same higher-order-moment framework for estimation. As the mid-spectrum using Gabor wavelets does not fit the sum-of-Gaussians model, the corresponding results are not reasonable at all.

which is symmetric in the spectral domain. Now we sample the positive spectral space with Gabor wavelets and skew Gabor filters. We start the mid-frequency at $\omega_0 = \pi/128$ and increase it with a fine step of $\pi/128$. The mid-spectra of both filters are clearly displayed due to the dense sampling. Here we set the highest mid-frequency as $\omega_0 = 7\pi/8$ so that we do not need to consider the boundary problem in the discrete mid-spectrum. Although the spectrum of the input signal is a simple sum of two Dirac functions, the mid-spectra using both filters are so blurred that it is hard to identify the source signals by direct observation (see Fig. 7). The positive skewness in applying Gabor wavelets even makes it impossible to apply deblurring methods. In contrast, after correcting the skewness we can estimate the amplitudes and the locations of two positive Dirac components analytically using higher order moment information (cf. Eq. (21)). The estimation results are very close to the true values (see Table 1). For comparison, we also extract higher order moment information blindly from the mid-spectrum after Gabor wavelets filtering and use Eq. (21) again for estimation. As the sum-of-Gaussians model is no more valid, the estimation results are far away from the true values, as shown in Table 1 as well.

In the negative frequencies, we may perform a similar procedure to extract the desired parameters. Then, we are able to identify the source signal components in spite of the blurring in the mid-spectrum. In other words, this method can "deblur" the mid-spectrum.

Taking into account that a lot of efforts had to be made in filter design so that the blurring after filtering does not significantly affect the identification of signals or orientations (e.g. [23,27,29]), this framework provides an elegant solution to improve the resolution in the mid-frequency space.

4. Spectral orientation analysis in the 2D spatial-temporal space

In this section, we analyze multiple orientations in the 2D spectral space. This has important applications in 1D multiple motion estimation. According to [11,12,2,30],

both 1D occlusion and transparency may be modelled as energy concentration along multiple lines passing through the origin in the spectral domain with some energy distortion in the case of occlusion and without any distortion in the case of transparency. The normal vectors of these spectral lines denote motion parameters. Thus, the problem of motion estimation turns out to be orientation analysis in the Fourier space. Determining the orientation of spectral lines, however, is a challenging task since the angle between two spectral lines can be arbitrary. Eigenvalue analysis (e.g. [26,17]) cannot properly determine the orientation of multiple lines. Sampling the spectrum with Gabor wavelets provided a good motivation, but suffered under the limited resolution. Here we prove that this limitation can be overcome using skew Gabor filters.

To simplify the spectral orientation analysis, we focus on the angular distribution of the energy spectrum. The polar integration of the spectral lines in the energy spectrum along the radial direction[1] yields the sum of two Dirac components

$$s(\theta) = a_1 \delta(\theta - \theta_1) + a_2 \delta(\theta - \theta_2). \qquad (24)$$

Here θ_1 and θ_2 denote the orientation of the spectral lines, and a_1 and a_2 represent the energy concentration of the spectral lines.

This equation reminds us of the similarity between 2D orientation analysis and 1D source signal separation (cf. Eq. (16)). Now we need to check if the polar integration of the 2D mid-spectrum also gives us the nice angular distribution fitting the sum-of-Gaussians model. The mid-spectrum after 2D Gabor wavelets filtering consists of differently-weighted non-symmetric skewness-surfaces concentrating along the spectral lines. Obviously, the corresponding angular distribution would not be symmetric and therefore, would not fit the sum-of-Gaussians model. In contrast, the mid-spectrum after skew Gabor filtering consists of 2D Gaussians concentrating along the spectral lines—the skewness has been corrected. The remaining question is whether the symmetric angular distribution is a sum of Gaussians. In order to answer this question, we first study the angular distribution of one 2D Gaussian.

For a 2D Gaussian centered at $O_i = (\omega_{x,i}, \omega_{ti})$ (cf. Fig. 8), its angular distribution reads
(see Appendix C for detail)

$$\begin{aligned}
sh_a(\theta) = &\frac{1}{2\pi} \exp\left\{ -\frac{C^2}{2} \right\} + \frac{C}{2\sqrt{2\pi}} \cos(\theta - \theta_i) \\
&\times \exp\left\{ -\frac{C^2 \sin^2(\theta - \theta_i)}{2} \right\} \\
&\times \left\{ 1 + \mathrm{erf}\left(\frac{C}{\sqrt{2}} \cos(\theta - \theta_i) \right) \right\},
\end{aligned} \qquad (25)$$

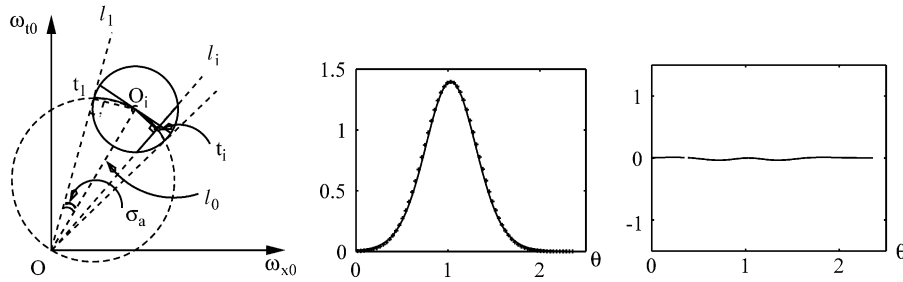[1] This integration is well known as Radon Transform [25].

Fig. 8. Left: The polar integration of an isotropic Gaussian centered at $O_i = (\omega_{xi}, \omega_{ti})$ can be approximated by an ideal Gaussian function $N(\theta_i, \sigma_a)$. The solid circle represents the support of the Gaussian. The pencil of lines passing through the origin denotes the integration paths. The middle point of the intersection between a integration path and the solid circle lies on the dotted circle passing through the origin and θ_i. Middle: The solid curve is the plot of $sh_a(\theta)$ (see Eq. (25) with $C = 3.5$ and ($\theta_i = \arctan(5/3)$). It is very similar to the Gaussian $N(\theta_i, \sigma_a)$. For comparison we plot the Gaussian with crosses as well. The scale of this Gaussian is $\sigma_a = \sin^{-1}(1/C)$. Right: The difference between $sh_a(\theta)$ and $N(\theta_i, \sigma_a)$. The maximal difference is less than 2% of $sh_a(\theta_i)$.

where θ_i is the polar angle of the Gaussian center $(\omega_{xi}, \omega_{ti})$ and $\mathrm{erf}(x)$ is the error integral function defined as

$$\mathrm{erf}(x) = \frac{2}{\sqrt{\pi}} \int_0^x e^{-t^2} \, dt.$$

This expression is symmetric with respect to the angle θ_i and has its maximum there. At a first sight, it is rather complicated. But it has only one parameter C. Further, the only difference between the polar integration and the marginal integration of a 2D Gaussian is the integration path: the polar integration paths go along the radial direction, while the marginal integration paths go in a parallel direction. It is known that the marginal integration of a 2D Gaussian is a 1D Gaussian. Therefore, it is reasonable to guess that Eq. (25) can be approximated by a Gaussian $N(\theta_i, \sigma_a)$, especially when the polar integration paths are close to be parallel.

In order to determine the scale parameter σ_a of the Gaussian, we turn to the geometric aspect of this approximation. In Fig. 8, we represent the support of a 2D isotropic Gaussian centered at O_i with a solid circle. The radius r_i of this circle is proportional to the scale of the Gaussian $\sigma_C = \sqrt{\omega_{xi}^2 + \omega_{ti}^2}/C$. For the simplicity of the following analysis we set $r_i = \sigma_C$. The lines passing through the origin $(1\_1, \cdots, 1\_i, \cdots)$ represent the paths of polar integration. Along each path, the linear segment between two intersection points on the solid circle forms a chord of the circle. It is not difficult to verify that the middle point t_i of the chords lie on another circle passing through the origin O and O_i, i.e. the dotted circle in Fig. 8. Correspondingly, the distance between O_i and t_i changes after the arc between them on the dotted circle. In other words, the remaining variable after polar integration varies non-linearly along the arc on the dotted circle. In the marginal integration of a 2D Gaussian with the integration paths parallel to l_0 in Fig. 8, the variable of the resulting 1D Gaussian changes linearly on the line perpendicular to l_0, as shown by the solid diameter passing through O_i. From the variable perspective, this difference explains why the polar

integration of a 2D Gaussian is not exactly a 1D Gaussian.

On the other side, however, we also observe that the arc variable is a good approximation of the diameter axis near the point O_i, especially if C is adequately large (e.g. $C = 3.5$). Thus, the angular distribution $sh_a(\theta)$ can be approximated by a Gaussian function with an appropriate scale parameter σ_a. From Fig. 8 it is clear that σ_a is equal to the angle between l_0 and l_1. As r_i is perpendicular to the tangent line l_1 at the tangent point t_1, we have

$$\sin(\sigma_a) = \frac{|r_i|}{|l_0|} = \frac{1}{C}. \tag{26}$$

Thus,

$$\sigma_a = \sin^{-1}\left(\frac{1}{C}\right). \tag{27}$$

The angle σ_a can be used to describe the approximation error because it indicates the difference between the arc variable after the polar integration and the linear variable after the marginal integration. The larger the σ_a value is, the larger the approximation error (for the marginal integration, this angle equals to zero). Eq. (27) also points out that σ_a is a function of C. Thus, we come to the conclusion that the approximation error can be controlled by C. Note that the distance between the Gaussian center O_i and the origin O does not play a role here in determining the approximation error when C is fixed. For the example shown in Fig. 8 with $C = 3.5$, the maximal difference between $sh_a(\theta)$ and $N(\theta_i, \sigma_a)$ is less than 2% of the maximal amplitude of $sh_a(\theta)$ (i.e. $sh_a(\theta_i)$).

Now let us come to the angular distribution of the complete mid-spectrum after 2D skew Gabor filtering. As the mid-spectrum of two motions is a set of 2D Gaussians centered on two spectral lines, the polar integration of the mid-spectrum along each spectral line is then a sum of 1D Gaussians with the same mean value and the same scale parameter σ_a. Consequently, the angular distribution of the mid-spectrum is the superposition of two 1D Gaussians and we are able to analyze 2D orientation with the framework introduced in Section 3. The only difference here is that

the parameter σ_a is no more proportional to θ_i, but a constant determined by C. Mathematically, the superposition of two angular Gaussians reads

$$g_a(\theta) = a_1 e^{(-(\theta-\mu_1)^2/2\sigma_a^2)} + a_2 e^{(-(\theta-\mu_2)^2/2\sigma_a^2)}. \qquad (28)$$

Here our goal is to determine four unknowns a_1 a_2, μ_1 and μ_2. According to the derivation in Appendix D, we have the following equation system

$$\begin{cases} a_1 + a_2 = \dfrac{m_0}{\sqrt{2\pi}\sigma_a} = b_1^* \\ a_1\mu_1 + a_2\mu_2 = \dfrac{m_1 m_0}{\sqrt{2\pi}\sigma_a} = b_2^* \\ a_1\mu_1^2 + a_2\mu_2^2 = \dfrac{(m_2 - \sigma_a^2)m_0}{\sqrt{2\pi}\sigma_a} = b_3^* \\ a_1\mu_1^3 + a_2\mu_2^3 = \dfrac{(m_3 - 3\sigma_a^2 m_1)m_0}{\sqrt{2\pi}\sigma_a} = b_4^* \end{cases}, \qquad (29)$$

where m_0 denotes the integration of $g_a(\theta)$ and m_1, m_2, and m_3 denote the first three order moments of $g_a(\theta)/m_0$. The solutions of this system read (see Appendix D for detail)

$$\begin{cases} a_1 = \dfrac{b_1^*\sqrt{(b^*)^2 - 4a^*c^*} + b^*b_1^* + 2a^*b_2^*}{2\sqrt{(b^*)^2 - 4a^*c^*}} \\ a_2 = \dfrac{b_1^*\sqrt{(b^*)^2 - 4a^*c^*} - b^*b_1^* - 2a^*b_2^*}{2\sqrt{(b^*)^2 - 4a^*c^*}} \\ \mu_1 = \dfrac{-b^* + \sqrt{(b^*)^2 - 4a^*c^*}}{2a^*} \\ \mu_2 = \dfrac{-b^* - \sqrt{(b^*)^2 - 4a^*c^*}}{2a^*} \end{cases}, \qquad (30)$$

where a^*, b^*, and c^* are defined as

$$\begin{cases} a^* = (b_2^*)^2 - b_1^*b_3^* \\ b^* = b_1^*b_4^* - b_2^*b_3^* \\ c^* = (b_3^*)^2 - b_2^*b_4^* \end{cases}. \qquad (31)$$

Now we obtain the orientation of the spectral lines analytically, even when the mid-spectrum is blurred. The normal vectors of these spectral lines further indicate the velocities of multiple motions.

5. Evaluation

To evaluate the performance of our framework, we use two synthetic examples with known ground truth and one real example. The first example demonstrates the deblurring ability of our framework. We synthesize a 2D signal whose spectrum is composed of two spectral lines passing through the origin (Fig. 9). The polar angles of these two lines are 30 and 60°, respectively. The mid-spectra after Gabor wavelets filtering and skew Gabor filtering are both strongly blurred so that the source signals are hardly to recognize in the mid-spectra. For comparison, we apply the same higher-order-moment framework on the polar integration results of both mid-spectra. The estimated polar angles are listed in Table 2 together with the true values. Clearly, the results from skew Gabor filtering is superior to the results from Gabor wavelets filtering.

The second example is to estimate motion parameters from a 1D transparency sequence, which is the simple overlapping of two source signals. We set the velocities of two source signals as -0.33 [pixel/frame] and -1 [pixel/frame], respectively. Correspondingly, the polar angles of two spectral lines are 18.43 and 45.00°. Note that the spatial periodicity of discrete Fourier transform (DFT) cannot be fulfilled for such a non-harmonic image. Consequently, we observe the aliasing effect after applying DFT directly on the original signal, as shown in Fig. 10. In order to avoid the aliasing problem, we low-pass the signal before starting the spectral-sampling. Similar to the first example, the mid-spectra after both Gabor wavelets filtering and skew Gabor filtering are displayed in Fig. 10. After the polar integration of the mid-spectra, we use the higher-order-moment framework to estimate the polar angles of the original spectral lines and further use the equation $v = \cot(\mu - 90°)$ to estimate the velocities of the source signals. Table 3 shows clearly that the polar angles of the spectral lines and the estimated velocities after Gabor wavelets filtering are far away from the true values, while skew Gabor filtering provides reasonable results.

In order to check the performance of the higher-order-moment framework under the affection of spectral distortion, we also use a 1D occlusion sequence with the same motion parameters as the transparency sequence. The difference between occlusion and transparency is that occlusion involves a step function in the spatial domain-thus causing the distortion in the spectral domain, while transparency is the simple overlapping of two source signals both in the spatial domain and in the spectral domain [30]. This difference is also shown in Fig. 11, where we can clearly observe the energy distortion of occlusion. The mid-spectra of the source signals are more disturbed and their normalized angular distributions have significant energy everywhere. As a result, the simple sum-of-Gaussians model is no more valid. If we still use the higher-order-moment framework on the angular distribution of the mid-spectra, the estimation results are not reliable at all, as shown in Table 3 as well. Improving the robustness against the noise is one of the topics in the future work.

The second example shows that the sum-of-Gaussians model cannot be used in the analysis of occlusion sequences. Therefore, we only use a real transparency sequence in the following to further compare Gabor wavelets and skew Gabor filters. Fig. 12 shows an image sequence consisting of a right-moving portrait and a left-moving package mirrored on the frame of the portrait. Since both motions are horizontal, we can simplify the motion estimation problem in the 2D sequence as an estimation in the 1D sequence by cutting a X–T plane through the image sequence, as shown in the first row of Fig. 12. In the X–T
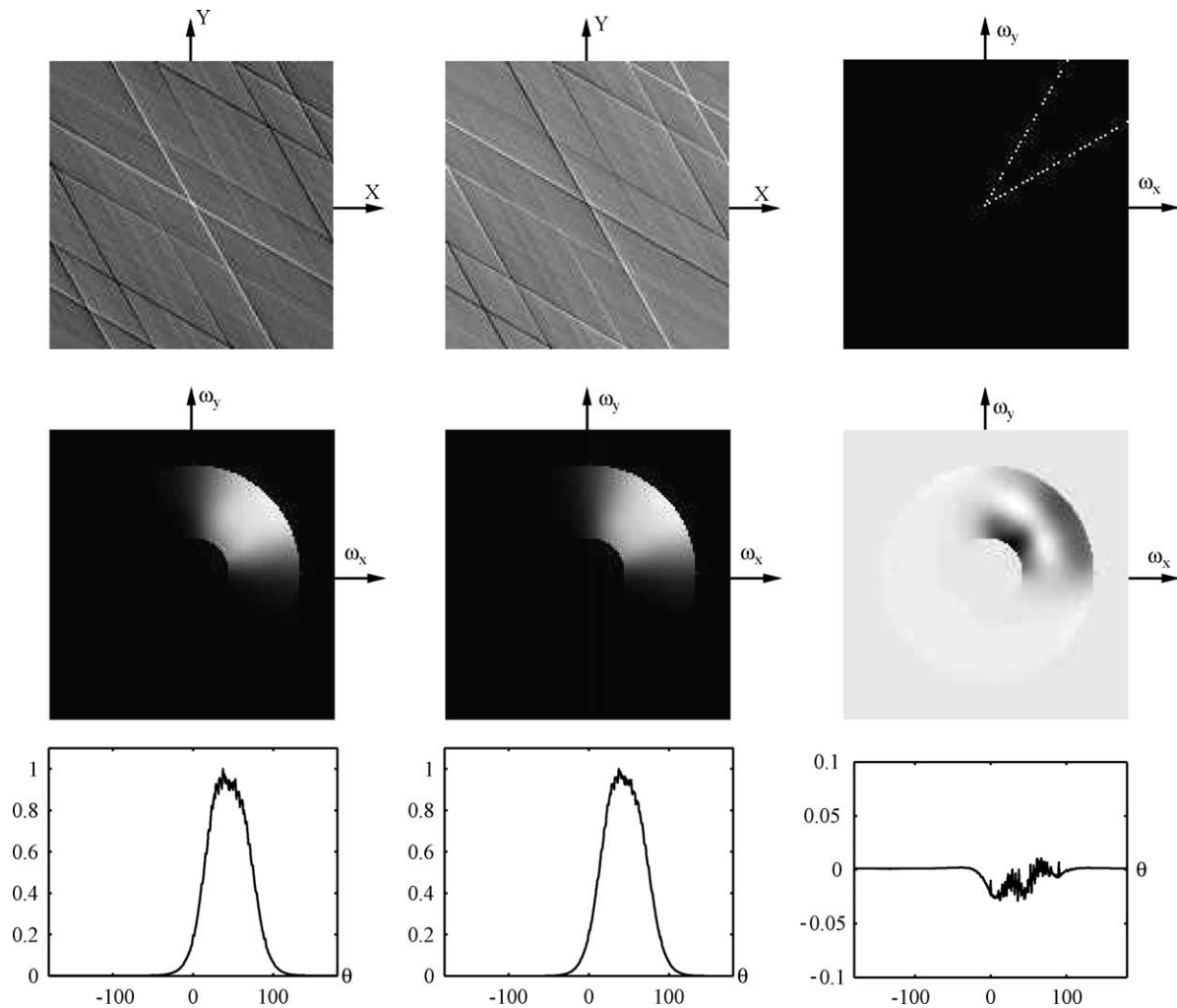
Fig. 9. Row 1: The real part (left), the imaginary part (middle), and the energy spectrum (right) of a 2D signal. The polar angles of two lines in the spectrum are 30 and 60°, respectively. Row 2:The mid-spectra using 2D Gabor wavelets (left) and skew Gabor filters (middle) with $C=3.5$ and their difference (right). The mid-frequency satisfies $\pi/4 \leq \sqrt{\omega_{x0}^2 + \omega_{t0}^2} \leq 3\pi/4$. Row 3: Normalized angular distributions of the mid-spectra (left: Gabor wavelets; middle: skew Gabor filter) and their difference (right). Note that the difference image has a smaller scale.

plane, we observe two motions as two oriented structures. In the 64×64 white window, we take the DFT directly and obtain the energy spectrum (row 1 right in Fig. 12). As the two motions are almost constant in the window, we are surprised to observe that some energy components locate outside the expected spectral lines. After careful study of the spatial-temporal image, we find out that the energy components lying horizontally outside the spectral lines are caused by noise and the aliasing effect of DFT, while the temporal intensity variations are responsible for the vertical energy bar (The dominant temporal variations are three black horizontal lines above the white window (cf. row 1 middle in Fig. 12). There are also some almost invisible dark lines lying horizontally in the window). Fortunately, the energy level of these disturbing components is much lower than the energy level of those components concentrating along the spectral lines (cf. row 3 in Fig. 12). Thus, we still can use the sum-of-Gaussians model to estimate

the polar angles of the spectral lines, although we are aware of the possible bias caused by the noise.

The real problem is that we do not know the ground truth about the motions, which makes the comparison difficult. Fortunately, the motions in the white window are almost constant. Thus, we can extract the motion parameters roughly by measuring the structure orientation. The polar angles of two structures are 69.44 and 108.43° with an angle

Table 2
Estimation results on Mid-Spectra using Gabor wavelets and skew Gabor filters

Parameter	True value	Gabor wavelets filtering	Skew Gabor filtering
μ_1 (°)	30	11.39	26.50
μ_2 (°)	60	55.72	62.19

For comparison we apply the same higher-order-moment framework for estimation. Skew Gabor filtering provides resonables results, while Gabor wavelets cannot.
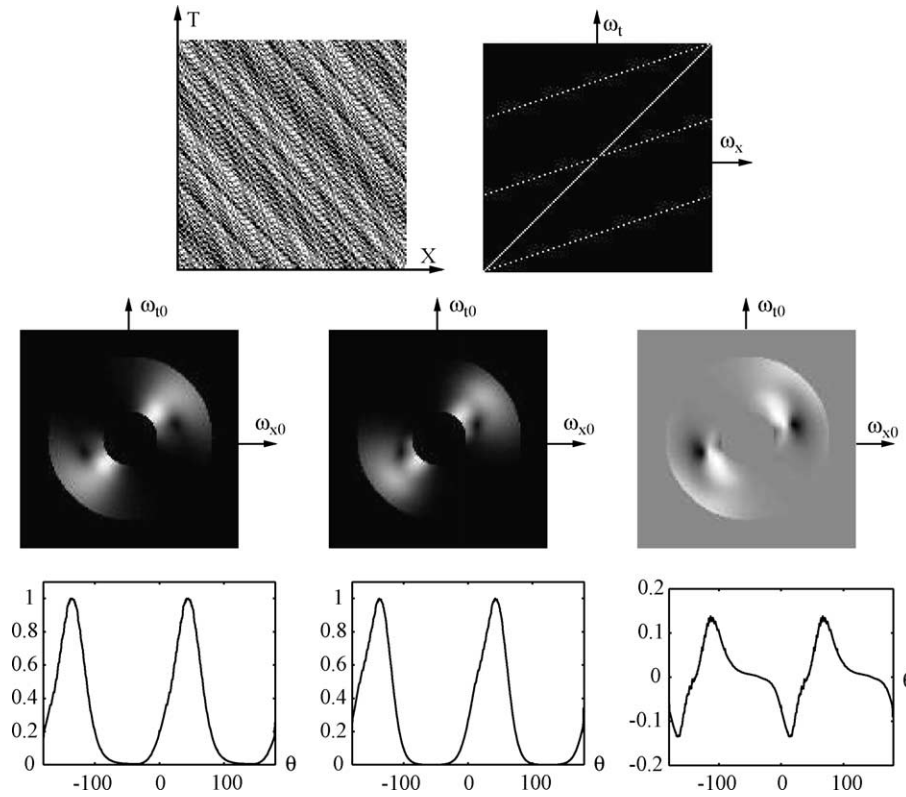
Fig. 10. Row 1: The 1D random dot transparency sequence (left) and its energy spectrum after applying DFT directly. The motion parameters are $v_1 = -0.33$ [pixel/frame] and $v_2 = -1.00$ (pixel/frame). Here the signals are moving toward the negative direction of the X-axis. The overlapping of two source signals form oriented structures in the spatial-temporal plane. Row 2: The mid-spectra after Gabor wavelets filtering (left) and skew Gabor filtering (middle). Their difference is shown on the right. Row 3: The normalized angular distributions corresponding to the mid-spectra and their difference. The estimated polar angles of the spectral lines are listed in Table 3.

of 38.99° between them. According to the Fourier analysis, the polar angles of two spectral lines are -20.56 and 18.43°, respectively. The angle between them is the same as in the spatial domain since the Fourier transform is an isometric mapping. Table 4 shows that the skew Gabor filter provides results closer to the measured values than Gabor wavelets. However, the difference between the skew Gabor filter and Gabor wavelets is not significant comparing to the difference in the random dot transparency example. For this phenomenon we have the following explanations:

• The energy spectrum in the white window is not a pure overlap of two spectral lines. The visible energy components outside the spectral lines bias the sum-of-Gaussians model. This explains why we cannot obtain the perfect results using the skew Gabor filter.
• The spectral lines in the energy spectrum happen to be nearly symmetric about the ω_x-axis, while the skewness of each spectral line after Gabor wavelets filtering (cf. Eq. (10)) appears in the direction leaving the ω_{x0}-axis. In other words, the skewness surfaces of both

Table 3
Estimation results in both transparency and occlusion sequences

Sequence	Parameter	True value	Gabor wavelets	Skew gabor filter
Transparency	μ_1	18.43°	26.32°	16.38°
	μ_2	45.00°	58.98°	45.74°
	$v_1 = \cot(\mu_1 - 90°)$	-0.33	-0.49	-0.29
	$v_2 = \cot(\mu_2 - 90°)$	-1.00	-1.66	-1.03
Occlusion	μ_1	18.43°	2.47°	4.41°
	μ_2	45.00°	92.11°	90.68°
	$v_1 = \cot(\mu_1 - 90°)$	-0.33	–	–
	$v_2 = \cot(\mu_2 - 90°)$	-1.00	–	–

In the transparency sequence, the sum-of-Gaussians model is valid for the angular distribution of the mid-spectrum after skew Gabor filtering. Thus, we obtain reasonable estimation results. A blind application of the same framework on the mid-spectrum after Gabor wavelets filtering shows that the results are far away from the true values. In the occlusion sequence, the sum-of-Gaussians model is fragile under the affection of the distortion so that the estimated polar angles of spectral lines are no more reasonable. As a result, the estimated motion parameters v_1 and v_2 are not reliable.
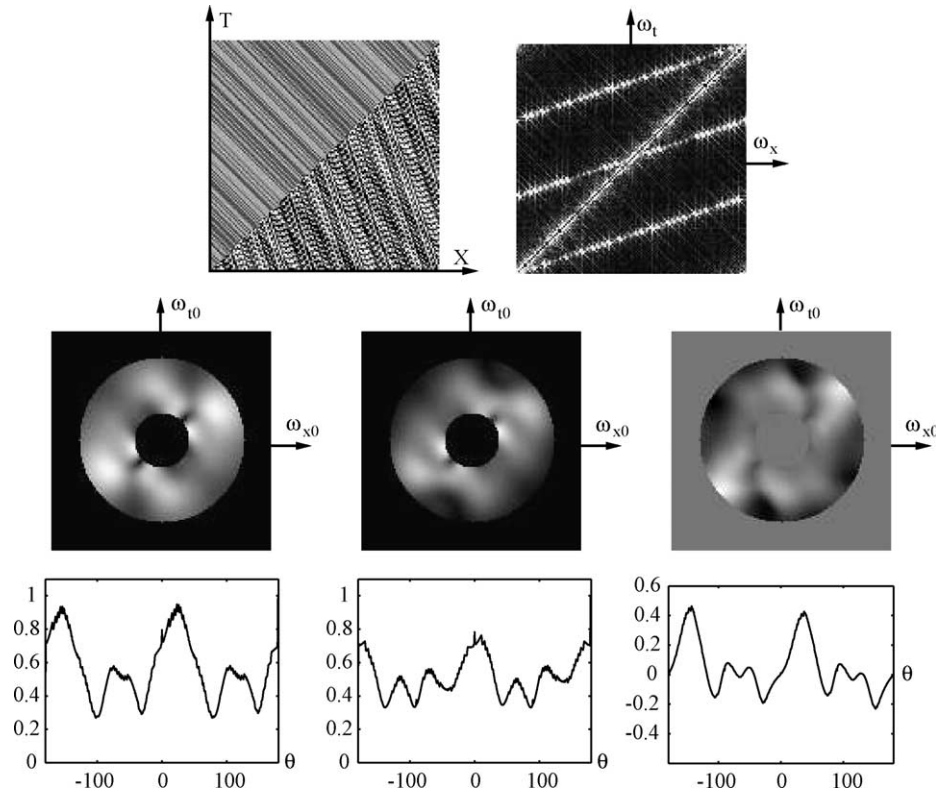
Fig. 11. Row 1: The 1D random dot occlusion sequence (left) with the same motion parameters as the 1D transparency sequence in Fig. 10. The occlusion boundary is moving toward the positive direction of the *X*-axis. The energy spectrum (right) after the DFT is disturbed by the distortion. Row 2: The mid-spectra after Gabor wavelets filtering (left) and skew Gabor filtering (middle). The energy is less concentrated than the energy in the transparency sequence due to the distortion. The difference of two mid-spectra is shown on the right. Row 3: The normalized angular distributions corresponding to the mid-spectra and their difference. The minimal energy component is much higher than its counterpart in Fig. 10. The estimated polar angles of the spectral lines are listed in Table 3.

spectral lines happen to be nearly symmetric about the ω_{x0}-axis—the skewness in the mid-spectrum has been cancelled out due to the symmetric properties of the spectral lines (This analysis can be proved by the angular distribution of the mid-spectrum in Fig. 12). Without the skewness, the mid-spectrum after Gabor wavelets filtering is closer to the sum-of-Gaussians model. Thus, the results after Gabor wavelets filtering are almost comparable to those after skew Gabor filtering.

We can verify the first explanation by using the fact that the noise outside the spectral lines is close to an uniform distribution in the angular space. We can roughly suppress the energy of the noise by deducting a certain amount of energy everywhere. Denoting the angular energy distribution as $s0$, we replace $s0$ with $s0 - \min(s0)$ before applying the the higher-order-moment framework. This modification suppresses a large part of the energy components outside the spectral lines and the improvement of the estimation precision is sufficient to support the above explanation. Interestingly, the same adjustment also works for the symmetric mid-spectrum after Gabor wavelets filtering. Certainly we could not expect the ad hoc modification in this specific example works in general

cases because the energy distribution of noise is generally unknown. Also, the distortion in the occlusion example cannot be suppressed by this simple trick of energy deduction. A systematic solution to this problem remains open.

6. Conclusion and discussion

In this paper, we have proposed a new filter to correct the skewness of Gabor wavelets in the mid-frequency space. After the correction we are able to model the distribution in the parameter space with a sum of different Gaussian functions. Comparing with the non-symmetric skewness curves, the benefit of using Gaussian functions for distribution description is obvious: Gaussians have good localization ability and are capable of providing simple yet rich descriptions of signals. From the point of view of probabilistic signal processing and pattern recognition, this correction simplifies the tasks of signal analysis significantly. For example, the analytical framework for source signal separation benefits from the statistical simplicity of Gaussians in calculating higher order moments.
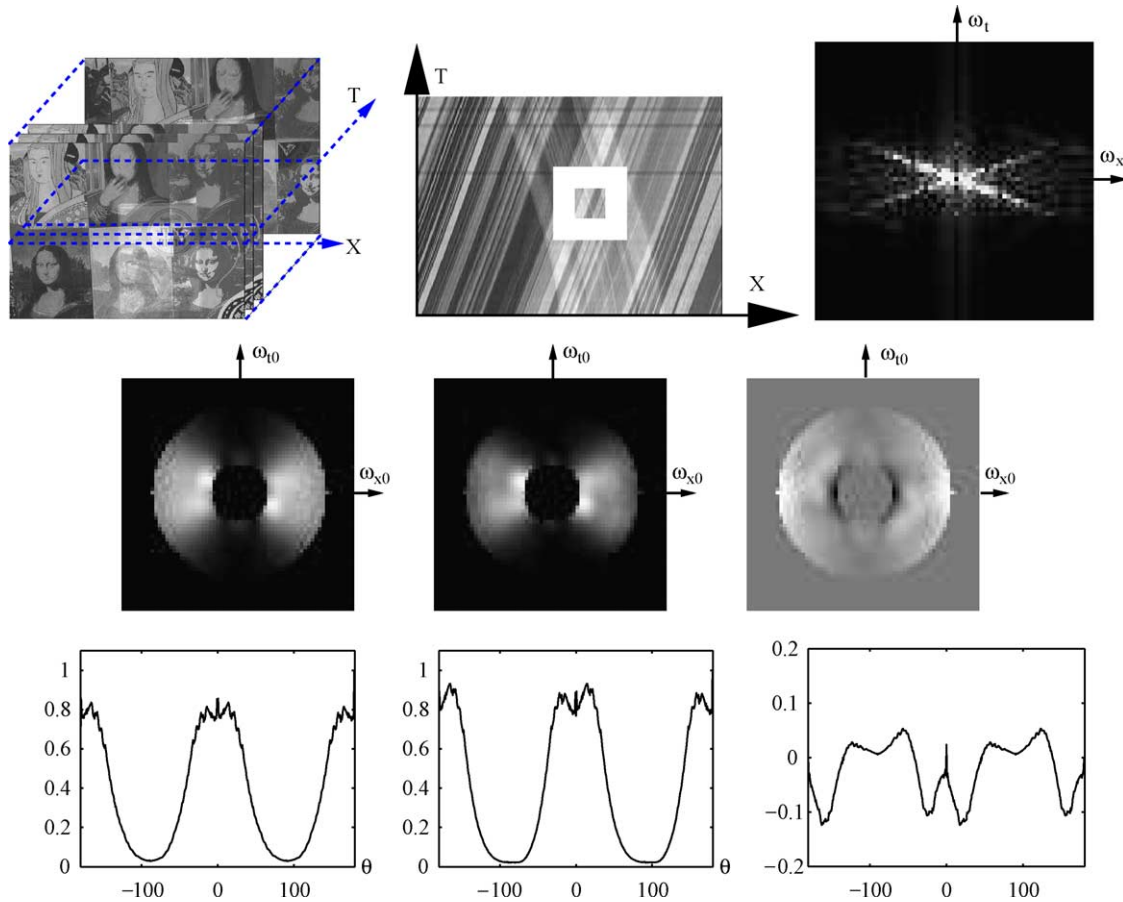
Fig. 12. Row 1 Left: Extracting an X–T plane from a real transparency sequence. Row 1 Middle: The X–T plane in detail with a white window denoting the location of local spectral analysis. Two motions are nearly constant inside the window. Row 1 Right: The energy spectrum of the signal in the white window after using DFT directly. The vertical energy bar is not a printing problem. It is caused by the temporal intensity variation in the white window (cf. Row 1 Middle). Row 2: The mid-spectra after Gabor wavelets filtering (left) and skew Gabor filtering (middle) and their difference (right). Row 3: The normalized angular distribution of the mid-spectra (left: Gabor wavelets; middle: skew Gabor filter; right: their difference). The estimated polar angles of the spectral lines are listed in Table 4.

Higher order moment information is also used in independent component analysis (ICA) approaches [5,10]. In ICA approaches we need a numerical solution (e.g. singular value decomposition (SVD)) because the distribution is unknown. In our framework, however, the sum-of-Gaussians model makes an analytic solution possible.

Another point of our source signal separation framework is that most frequency-based methods suffer from low resolution (e.g. [30]) due to spreading and overlapping.

By achieving the spreading to have a Gaussian shape, we can separate two overlapping Gaussians in the mid-frequency space. This enables us to reach very fine resolution in the spectral domain and eventually solve the aliasing problem.

The higher-order-moment framework can only separate two Gaussian functions. This requires that the source signal should have no more than two harmonic components. Under the affection of noise with even low energy level,

Table 4
Measured and estimated parameter values in the real transparency sequence

Parameter	True value	GW	GWWED	SG	SGWED
μ_1 (°)	≈ -20.56	-26.27	-23.38	-22.97	-20.36
μ_2 (°)	≈ 18.43	26.83	24.42	25.29	23.69
$v_1 = \cot(\mu_1 - 90°)$	≈ 0.37	0.49	0.43	0.42	0.37
$v_2 = \cot(\mu_2 - 90°)$	≈ -0.33	-0.51	-0.45	-0.47	-0.44
$\mu_2 - \mu_1$ (°)	≈ 38.99	53.10	47.80	48.26	44.05

The results using skew Gabor filtering are closer to the measured values than the results using Gabor wavelets filtering. But these results are not perfect due to the affection of energy components outside the spectral lines in Fig. 12 If we suppress these energy components by deducting the amount of the minimal component from each term in the angular distribution, the results are then improved. Here GW denotes Gabor wavelets, GWWED denotes Gabor wavelets with energy deduction, SG means skew Gabor filter, and SGWED means skew Gabor filter with energy deduction.

the number of source signal components is easily over two and causes the higher-order-moment framework to have a poor performance. In order to improve the robustness against noise and eventually extend the range of applications (e.g. occlusion analysis), we must either extend the allowable number of source components or develop a new optimization framework to suppress the noise.

In this paper, we limit our application in the 2D spatial-temporal space. We plan to extend the current framework to the 3D spatial-temporal space to analyze multiple motions in the real world, in which the spectral lines turn out to be spectral planes. With the increase of dimension, the computational complexity problem also needs to be addressed. We may reduce the computational load by using elongated filter kernels to sample the mid-frequency space more efficiently and by studying how sparsely we can sample the spectrum without affecting the parameter regression.

Appendix A

For convenience we change the variable in Eq. (18) to x

$$g(x) = a_1 e^{-(x-\mu_1)^2/(2(\mu_1/C))^2} + a_2 e^{-(x-\mu_2)^2/(2(\mu_2/C))^2}.$$

In order to use moments, we must normalize $g_1(x)$, $g_2(x)$, and $g(x)$ to obtain the corresponding distribution density functions $f_1(x)$, $f_2(x)$, and $f(x)$:

$$m_{01} = \int g_1(x)\mathrm{d}x = \frac{\sqrt{2\pi}}{C}a_1\mu_1,$$

$$m_{02} = \int g_2(x)\mathrm{d}x = \frac{\sqrt{2\pi}}{C}a_2\mu_2,$$

$$m_0 = \int g(x)\mathrm{d}x = \frac{\sqrt{2\pi}}{C}(a_1\mu_1 + a_2\mu_2),$$

$$f_1(x) = \frac{1}{m_{01}}g_1(x) = \frac{1}{\frac{\sqrt{2\pi}}{C}\mu_1}e^{-((x-\mu_1)^2/2(\mu_1/C)^2)},$$

$$f_2(x) = \frac{1}{m_{02}}g_2(x) = \frac{1}{\frac{\sqrt{2\pi}}{C}\mu_2}e^{-((x-\mu_2)^2/2(\mu_2/C)^2)},$$

$$f(x) = \frac{1}{m_0}g(x) = \frac{1}{a_1\mu_1 + a_2\mu_2}[a_1\mu_1 f_1(x) + a_2\mu_2 f_2(x)].$$
(A1)

The first three order moments of $f(x)$ read

$$m_1 = \int x f(x)\mathrm{d}x = \frac{1}{a_1\mu_1 + a_2\mu_2}(a_1\mu_1^2 + a_2\mu_2^2), \quad \text{(A2)}$$

$$m_2 = \int x^2 f(x)\mathrm{d}x = \frac{\frac{1}{C^2}+1}{a_1\mu_1 + a_2\mu_2}(a_1\mu_1^3 + a_2\mu_2^3), \quad \text{(A3)}$$

$$m_3 = \int x^3 f(x)\mathrm{d}x = \frac{\frac{3}{C^2}+1}{a_1\mu_1 + a_2\mu_2}(a_1\mu_1^4 + a_2\mu_2^4). \quad \text{(A4)}$$

Reformulate Eqs. (A1)–(A4) yields the equation system (20).

Appendix B

After defining $x_1 = a_1\mu_1$, $x_2 = a_2\mu_2$, we get an equation system of variables x_1, x_2, μ_1, and μ_2 from (20)

$$x_1 + x_2 = b_1, \quad \text{(B1)}$$

$$x_1\mu_1 + x_2\mu_2 = b_2, \quad \text{(B2)}$$

$$x_1\mu_1^2 + x_2\mu_2^2 = b_3, \quad \text{(B3)}$$

$$x_1\mu_1^3 + x_2\mu_2^3 = b_4. \quad \text{(B4)}$$

From (B1) and (B2) we obtain

$$x_1(\mu_1 - \mu_2) = b_2 - b_1\mu_2, \quad \text{(B1.1)}$$

$$x_2(\mu_1 - \mu_2) = b_1\mu_1 - b_2. \quad \text{(B2.1)}$$

We multiply both sides of (B3) and (B4) with $(\mu_1 - \mu_2)$ and simplify them as

$$(b_2 - b_1\mu_1)\mu_2 = b_3 - b_2\mu_1, \quad \text{(B3.1)}$$

$$(b_2 - b_1\mu_1)\mu_2^2 + (b_2 - b_1\mu_1)\mu_1\mu_2 + b_2\mu_1^2 - b_4 = 0. \quad \text{(B4.1)}$$

Submit (B3.1) into (B4.1) yields

$$a\mu_1^2 + b\mu_1 + c = 0 \quad \text{(B5)}$$

with

$$\begin{cases} a = b_2^2 - b_1 b_3 \\ b = b_1 b_4 - b_2 b_3 \, . \\ c = b_3^2 - b_2 b_4 \end{cases}$$

This is a standard one variable, two order equation whose discriminator reads

$$b^2 - 4ac = (b_1 b_4 - b_2 b_3)^2 - 4(b_2^2 - b_1 b_3)(b_3^2 - b_2 b_4)$$
$$= [a_1 a_2 \mu_1 \mu_2 (\mu_1 - \mu_2)^3]^2 \geq 0 \quad \text{(B6)}$$

The equality is attainable only when $\mu_1 = \mu_2$, i.e. when we have only one single Gaussian. Then we only need to use (A1) and (A2) directly to extract its amplitude and mean value. In case of $b^2 - 4ac > 0$, we have two real roots (without loss of generality we assume $\mu_1 < \mu_2$)

$$\begin{cases} \mu_1 = \dfrac{-b + \sqrt{b^2 - 4ac}}{2a} \\ \mu_2 = \dfrac{-b - \sqrt{b^2 - 4ac}}{2a} \end{cases} . \quad \text{(B7)}$$

Submitting μ_1 and μ_2 into (B1.1) and (B2.1) and further taking into account that $x_1 = a_1\mu_1$, $x_2 = a_2\mu_2$ we

solve a_1 and a_2

$$\begin{cases} a_1 = \dfrac{a(2ab_2 + bb_1 + b_1\sqrt{b^2 - 4ac})}{b^2 - 4ac - b\sqrt{b^2 - 4ac}} \\ a_2 = \dfrac{a(2ab_2 + bb_1 - b_1\sqrt{b^2 - 4ac})}{b^2 - 4ac + b\sqrt{b^2 - 4ac}} \end{cases} . \tag{B8}$$

Appendix C

In order to calculate the angular distribution of Gaussian function after polar integration we use the following knowledge

$$\int_{\theta=0}^{2\pi} \int_{r=0}^{\infty} sh_2(r, \theta, C) r \, \mathrm{d}r \, \mathrm{d}\theta$$

$$= \int_{\omega_{x0}} \int_{\omega_{t0}} sh_2(\omega_{x0}, \omega_{t0}, C) \mathrm{d}\omega_{x0} \, \mathrm{d}\omega_{t0} = 2\pi \frac{\omega_{xi}^2 + \omega_{ti}^2}{C^2},$$

where $sh_2(r, \theta, C)$ is the polar representation of $sh_2(\omega_{x0}, \omega_{t0}, C)$. Using the polar mapping $(\omega_{xi}, \omega_{ti}) \to (r_i, \theta_i)$ and $(\omega_{x0}, \omega_{t0}) \to (r, \theta)$ we have

$$sh_2(r, \theta, C) = \exp\left\{ -\frac{r^2 + r_i^2 - 2rr_i\cos(\theta - \theta_i)}{2r_i^2/C^2} \right\}$$

$$= \exp\left\{ -\frac{(r - r_i\cos(\theta - \theta_i))^2 + r_i^2\sin^2(\theta - \theta_i)}{2r_i^2/C^2} \right\}.$$

The radial integration yields

$$\int_{r=0}^{\infty} sh_2(r, \theta, C) r \, \mathrm{d}r = \exp\left\{ -\frac{C^2\sin^2(\theta - \theta_i)}{2} \right\}$$

$$\times \int_{r=0}^{\infty} \exp\left\{ -\frac{(r - r_i\cos(\theta - \theta_i))^2}{2r_i^2/C^2} \right\} r \, \mathrm{d}r \tag{C1}$$

As

$$\int_{r=0}^{\infty} \exp\left\{ -\frac{(r - r_i\cos(\theta - \theta_i))^2}{2r_i^2/C^2} \right\} r \, \mathrm{d}r$$

$$= \frac{r_i^2}{C^2} \exp\left\{ -\frac{C^2\cos^2(\theta - \theta_i)}{2} \right\}$$

$$+ \frac{\sqrt{2\pi} r_i^2\cos(\theta - \theta_i)}{2C} \left\{ 1 + \mathrm{erf}\left(\frac{C}{\sqrt{2}}\cos(\theta - \theta_i) \right) \right\},$$

Eq. (C1) turns out to be

$$\int_{r=0}^{\infty} sh_2(r, \theta, C) r \, \mathrm{d}r = \frac{r_i^2}{C^2} \exp\left\{ -\frac{C^2}{2} \right\} + \frac{\sqrt{2\pi} r_i^2\cos(\theta - \theta_i)}{2C}$$

$$\times \exp\left\{ -\frac{C^2\sin^2(\theta - \theta_i)}{2} \right\}$$

$$\times \left\{ 1 + \mathrm{erf}\left(\frac{C}{\sqrt{2}}\cos(\theta - \theta_i) \right) \right\}.$$

After the normalization with $2\pi(\omega_{xi}^2 + \omega_{ti}^2/C^2) = 2\pi(r_i^2/C^2)$ we have the angular distribution function

$$sh_a(\theta) = \frac{1}{2\pi}\exp\left\{ -\frac{C^2}{2} \right\} + \frac{C}{2\sqrt{2\pi}}\cos(\theta - \theta_i)$$

$$\times \exp\left\{ -\frac{C^2\sin^2(\theta - \theta_i)}{2} \right\}$$

$$\times \left\{ 1 + \mathrm{erf}\left(\frac{C}{\sqrt{2}}\cos(\theta - \theta_i) \right) \right\}.$$

Appendix D

To follow the derivation in Appendices A and B, we change the variable in Eq. (28) to x

$$g_a(x) = a_1 e^{-((x-\mu_1)^2/2\sigma_a^2)} + a_2 e^{-((x-\mu_2)^2/2\sigma_a^2)}. \tag{D1}$$

Similar to (A1)–(A4), the integration of $g_a(x)$ (i.e. m_0) and the first three order moments of $g_a(x)/m_0$ read

$$m_0 = \sqrt{2\pi}\sigma_a(a_1 + a_2), \tag{D2}$$

$$m_1 = \frac{1}{a_1 + a_2}(a_1\mu_1 + a_2\mu_2), \tag{D3}$$

$$m_2 = \frac{1}{a_1 + a_2}(a_1\mu_1^2 + a_2\mu_2^2) + \sigma_a^2, \tag{D4}$$

$$m_3 = \frac{1}{a_1 + a_2}(a_1\mu_1^3 + a_2\mu_2^3) + 3\sigma_a^2 m_1. \tag{D5}$$

Reformulating (D2)–(D5) yields the equation system (29). This equation system is the same as (B1)–(B4). We may simply get the solutions of μ_1 and μ_2 from (B7)

$$\begin{cases} \mu_1 = \dfrac{-b^* + \sqrt{(b^*)^2 - 4a^*c^*}}{2a^*} \\ \mu_2 = \dfrac{-b^* - \sqrt{(b^*)^2 - 4a^*c^*}}{2a^*} \end{cases} . \tag{D6}$$

with

$$\begin{cases} a^* = (b_2^*)^2 - b_1^* b_3^* \\ b^* = b_1^* b_4^* - b_2^* b_3^* \\ c^* = (b_3^*)^2 - b_2^* b_4^* \end{cases} . \tag{D7}$$

Substituting (D6) into (B1.1) and (B2.1) solves the rest two variables

$$\begin{cases} a_1 = \dfrac{b_1^*\sqrt{(b^*)^2 - 4a^*c^*} + b^* b_1^* + 2a^* b_2^*}{2\sqrt{(b^*)^2 - 4a^*c^*}} \\ a_2 = \dfrac{b_1^*\sqrt{(b^*)^2 - 4a^*c^*} - b^* b_1^* - 2a^* b_2^*}{2\sqrt{(b^*)^2 - 4a^*c^*}} \end{cases} . \tag{D8}$$

Thus, we get the solutions of these four unknowns.

References

[1] E.H. Adelson, J.R. Bergen, Spatiotemporal energy models for the perception of motion, Journal of Optical Society of America A 2 (2) (1985) 284–299.

[2] S.S. Beauchemin, J.L. Barron, The frequency structure of 1d occluding image signals, IEEE Transactions on Pattern Analysis and Machine Intelligence 22 (2000) 200–206.

[3] A.C. Bovik, M. Clark, W.S. Geisler, Multichannel texture analysis using localized spatial filters, IEEE Transactions on Pattern Analysis and Machine Intelligence 12 (1990) 55–73.

[4] R.N. Bracewell, The Fourier Transform and Its Applications, McGraw-Hill, New York, 1986.

[5] J. Cardoso, Source separation using higher order moments. In IEEE International Conference on Acoustics, Speech and Signal Processing, pp. 2109–2112, 1989.

[6] K. Daubechies. Ten Lectures on Wavelets. Society for Industrial and Applied Mathematics, 1992.

[7] J.G. Daugman, Uncertainty relation for resolution in space, spatial frequency and orientation optimized by two-dimensional visual cortical filters, Journal of the Optical Society of America 2 (7) (1985) 1160–1169.

[8] J.G. Daugman, An information-theoretic view of analog representation in striate cortex. In: E.L. Schwartz (Ed.), Computational Neuroscience, MIT Press, 1990, pp. 403–423.

[9] J.G. Daugman, Complete discrete 2-d Gabor transforms by neural networks for image analysis and compression, IEEE Transactions on Acoustics, Speech, and Signal Processing 36 (7) (1988).

[10] H. Farid, E.H. Adelson, Separating reflections from images using independent components analysis, Journal of the Optical Society of America 16 (9) (1999) 2136–2145.

[11] D.J. Fleet, Measurement of Image Velocity, Kluwer, Dordecht, 1992.

[12] D.J. Fleet, K. Langley, Computational analysis of non-Fourier motion, Vision Research 34 (1994) 3057–3079.

[13] D. Gabor, Theory of communication, Journal of the IEE 93 (1946) 429–457.

[14] N.M. Grzywacz, A.L. Yuille, A model for the estimate of local image velocity by cells in the visual cortex, Proceedings of the Royal Society of London, B 239 (1990) 129–161.

[15] D.J. Heeger, Optical flow using spatiotemporal filters, International Journal of Computer Vision 1 (4) (1988) 279–302.

[16] F. Heitger, L. Rosenthaler, R. Von der Heydt, E. Peterhans, O. Kuebler, Simulation of neural contour mechanisms: from simple to end-stopped cells, Vision Research 32 (5) (1992) 963–981.

[17] B. Jähne, Spatio-Temporal Image Processing, Springer, Berlin, 1993.

[18] A.K. Jain, F. Farrokhnia, Unsupervised texture segmentation using Gabor filters, Pattern Recognition 24 (12) (1991) 1167–1186.

[19] J.J. Koenderink, A.J. Van Doorn, Representation of local geometry in the vision system, Biological Cybernetics 55 (1987) 367–375.

[20] T.S. Lee, Image representation using 2D Gabor wavelets, IEEE Transactions on Pattern Analysis and Machine Intelligence 18 (10) (1996) 959–971.

[21] S.G. Mallat, A theory for multiresolution signal decomposition: The wavelet representation, IEEE Transactions on Pattern Analysis and Machine Intelligence 11 (7) (1989) 674–693.

[22] B.S. Manjunath, W.Y. Ma, Texture features for browsing and retrieval of image data, IEEE Transactions on Pattern Analysis and Machine Intelligence 18 (8) (1996) 837–842.

[23] M. Michaelis, G. Sommer, Junction classification by multiple orientation detection. In: J.O. Eklundh (Ed.), Proceedings of the Third European Conference on Computer Vision vol. I, Springer LNCS 800, Stockholm, Sweden, 1994, pp. 101–108.

[24] T. Poggio, F. Girosi, Networks for approximation and learning, Proceedings of the IEEE 78 (9) (1990) 1481–1497.

[25] J. Radon and translated by P.C. Parks, On the determination of functions from their integral values along certain manifolds, IEEE Transactions on Medical Imaging 5 (4) (1986) 170–176.

[26] M. Shizawa, K. Mase, A unified computational theory for motion transparency and motion boundaries based on eigenenergy analysis, In IEEE Conference on Computer Vision and Pattern Recognition, Maui, Hawaii 1991; 289–295.

[27] E.P. Simoncelli, H. Farid, Steerable wedge filters for local orientation analysis, IEEE Transaction on Image Processing 5 (9) (1996) 1377–1382.

[28] R.P. Würtz, Object recognition robust under translations, deformations, and changes in background, IEEE Transactions on Pattern Analysis and Machine Intelligence 19 (7) (1997) 769–774.

[29] W. Yu, K. Daniilidis, G. Sommer, Approximate orientation steerability based on angular Gaussians, IEEE Transactions on Image Processing 10 (2) (2001) 193–205.

[30] W. Yu, G. Sommer, S. Beauchemin, K. Daniilidis, Oriented structure of the occlusion distortion: Is it reliable?, IEEE Transactions on Pattern Analysis and Machine Intelligence 24 (9) (2002) 1286–1290.